Feedback regulation by the RhoA-specific GEF ARHGEF17 regulates actomyosin network disassembly

Vasundhara Rao [1,2], Benjamin Grädel [1,2*], Lucien Hinderling [1,2*], Jakobus Van Unen [1,3], Olivier Pertz [1]

[1] Institute of Cell Biology, University of Bern, 3012 Bern, Switzerland

[2] Graduate School for Cellular and Biomedical Sciences, University of Bern, Bern, Switzerland

[3] Projekt Epic, Schwarztorstrasse 96, 3007 Bern, Switzerland

[*] Both authors contributed equally

Abstract

We report that the RhoA-specific guanine nucleotide exchange factor ARHGEF17 localizes at the back of a fibroblast's contractile lamella and regulates its disassembly. This localization emerges through retrograde ARHGEF17 transport together with actomyosin flow that most likely involves interactions with ATP-actin at F-actin barbed ends. During this process, ARHGEF17 increasingly oligomerizes into clusters that co-localize with myosin filaments, and correlate with their disassembly at lamella's distal edge. ARHGEF17 loss of function leads to decreased RhoA activity at the lamella back and impairs its disassembly. High RhoA activity is however maintained at the lamella front where phosphorylated myosin light chain is observed. We propose that low levels of actomyosin network fracture at the lamella back generates barbed ends leading to generation of ATP-actin and ARHGEF17 binding, local activation of RhoA-dependent contractility, ensuring robust lamella disassembly. ARHGEF17

exemplifies the spatio-temporal complexity of Rho GTPase signaling and the requirement of feedback mechanism for homeostasis of contractile actomyosin networks.

Introduction

Rho GTPases regulate cytoskeletal dynamics essential for cell/tissue morphogenesis (Etienne-Manneville and Hall, 2002). Their (in)activation are orchestrated by GEFs and GTPase Activating Proteins (GAPs). In their GTP-bound state, Rho GTPases activate downstream effectors to modulate cytoskeletal dynamics. Initial studies, based on population-averaged activity measurements and dominant mutants involved Rac1 in lamellipodial extension, Cdc42 in filopodial protrusion, and RhoA in myosin-driven contractility.

Fluorescence Resonance Energy Transfer (FRET)-based biosensors unveiled more complex regulation (Itoh et al., 2002; Kraynov et al., 2000; Nalbant et al., 2004; Pertz et al., 2006) in which RhoA/Rac1/Cdc42 exhibit specific spatio-temporal signaling patterns that fluctuate on time scales of tens of seconds during leading edge protrusion/retraction cycles (Machacek et al., 2009). Adding to this complexity, distinct leading edge RhoA/Rac1/Cdc42 signaling patterns are observed at the leading edge upon application of promigratory cues (Martin et al., 2016). The finding of such complex spatio-temporal Rho GTPase signaling patterns must involve precise regulation by GEFs/GAPs. Signaling pattern formation involves a Rho GTPase flux consisting of sequential spatially regulated events such as GEF-triggered Rho GTPase GTP-loading, its diffusion within the plasma membrane, and GAP-mediated inactivation. Ubiquitous GEF/GAP expression, observed across cellular systems (Rossman et al., 2005), is consistent with this complexity.

Comprehensive screening of their subcellular localization revealed that many GEFs/GAPs bind to cytoskeletal and adhesion structures (Müller et al., 2020), suggesting the existence of feedback regulation. By example, Rac1-specific GEFs versus GAPs respectively localize to adhesion structures at the front versus the back of the leading edge. Thus, mechanical cues at adhesions at specific subcellular locations control the leading edge Rac activity gradient by spatially recruiting different GEFs/GAPs. Similarly, mechanosensitive interactions between the RhoGAP DLC1 and Talin allows its dissociation from focal adhesions under tension, locally increasing RhoA activity leading to positive feedback for robust and irreversible adhesion disassembly (Heydasch et al., 2023). Further, RhoGAP binding to F-actin provides spatial feedback shaping RhoA activity waves (Bement et al., 2024). Thus, interactions between GEFs/GAPs and cytoskeletal/adhesion structures provides feedback modalities that shape Rho GTPase signaling patterns. Traditional genetic manipulation techniques, which induce long-term changes in cellular states, do not adequately capture such spatio-temporal feedbacks. New methodologies are required to dynamically probe the Rho GTPase flux at adequate length and time scales in single cells.

Consistently with this signaling complexity, leading edge dynamics cycles involve two distinct yet interconnected structures, the lamellipodium and the lamella (Ponti et al., 2004; Small et al., 2002). The lamellipodium explores the environment, forming new protrusions and guiding the direction of movement. The lamella follows, consolidates protrusions into stable adhesions, and generates the contractile forces to pull the cell forward. This strongly suggests that multiple signaling modules must exist to spatio-temporally regulate these different cytoskeletal polymers.

Beyond Rho GTPase regulation, the self-organisation properties of the actomyosin cortex feed into regulation of morphogenetic processes. The actomyosin cortex can be understood as an active contractile matter that spontaneously form patterns such as waves, rings, or aggregates due to instabilities in the distribution of contractile forces (Salbreux et al., 2012). Experiments with isolated actomyosin systems have shown that the contractile activity of myosin motors can amplify small fluctuations in the distribution and alignment of actin filaments in a self-reinforcement manner that can result in structural changes such as buckling, fracturing or aggregate formation, that lead to tension loss (Ideses et al., 2018). Cells must therefore deal with emergence of potential catastrophic contractile instabilities in cells.

An interesting GEF that mediates crosstalk from the cytoskeleton to Rho GTPase signaling is the RhoA-specific GEF ARHGEF17, also known as Tumor Endothelial Marker 4 (Mitin et al., 2013, 2012). ARHGEF17 is characterized by an N-terminal actin-binding domain that exhibits a 90-fold higher affinity for ATP versus ADP-actin, and thus must bind to newly assembled F-actin filaments (Mitin et al., 2012; Prifti et al., 2022) (Fig. 1A). This is followed by a catalytic DH-PH domain, and a C-terminal WD40 propeller domain that might regulate protein-protein interactions. *In vitro* studies have shown that ARHGEF17 is specific for Rho isoforms (RhoA, RhoB, RhoC) over Rac1 and Cdc42 (Bagci et al., 2020; De Toledo et al., 2000; Mitin et al., 2012; Rümenapp et al., 2002a). This was later also found in a FRET biosensor assay that was used for mapping of the exchange specificities of all GEFs/GAPs in living cells (Müller et al., 2020). Expression of ARHGEF17 DH-PH domains leads to robust contractility (Mitin et al., 2012), further suggesting that it acts as a regulator of RhoA. ARHGEF17 therefore is highly likely to mediate cytoskeletal - Rho GTPase feedback, but the

102 function of this feedback in the spatio-temporal regulation of signaling remains
103 unclear.
104 Here, we show that ARHGEF17 dynamically localizes to the lamella back in spreading
105 REF52 fibroblasts. ARHGEF17 oligomerizes from small to larger clusters as it travels
106 with actomyosin retrograde flow. In the edge proximal lamella region, ARHGEF17
107 clusters sparsely bind to a highly contractile myosin network. In the edge distal lamella
108 region, that is characterized by low contractility, ordered ARHGEF17 cluster arrays
109 bind to transverse arcs, leading to disassembly of myosin filaments through their
110 fracture. ARHGEF17 knockdown (KD) leads to lack of lamella disassembly, impeding
111 symmetry breaking and polarization during spreading. On time scales of multiple
112 hours, this leads to a very contractile stress fiber network. Optogenetic perturbation of
113 contractility dynamics reveals that ARHGEF17 preferentially binds relaxing
114 actomyosin networks. As control cells, *ARHGEF17* KD cells still display a focused
115 RhoA activity pattern at the edge, that has been shown to regulate lamellar contractility
116 (Martin et al., 2016, 2014) . However, decreased RhoA activity is observed at the back
117 of this region, leading to lack of its disassembly. We propose that ARHGEF17 senses
118 ATP-actin at the actin filament barbed ends that are in a process of disassembly in the
119 low contractile edge distal lamella, and locally activate RhoA-mediated actomyosin
120 contractility as positive feedback to ensure efficient lamella disassembly.

121 **Results**

122
123 **ARHGEF17 binds to the edge distal region of the lamella during spreading**

124
125 To study feedback from the cytoskeleton to Rho GTPases, we evaluated the
126 subcellular localization of multiple GEPs and GAPs that were previously found to bind

127 to F-actin or adhesion structures in REF52 fibroblasts (Müller et al., 2020). Confocal
128 imaging of an exogenously-expressed GFP-tagged version of ARHGEF17
129 simultaneously together with F-actin staining, revealed that ARHGEF17 binds to the
130 edge distal lamella region, as well as binding to weakly stained F-actin
131 contractile structures in the middle of the cell (Figure 1B). Spinning disk confocal time-
132 lapse imaging of ARHGEF17 and MLC dynamics during cell spreading again revealed
133 a similar pattern (Figure 1C, Movie S1). Consistently with the fact that ARHGEF17
134 bears an actin binding domain (Mitin et al., 2012), it displayed retrograde flow together
135 with MLC (Movie S1). Within the central domain of the cell, ARHGEF17 dynamically
136 interacts with a contractile F-actin network with low MLC signal. Kymograph analysis
137 revealed that the lamella exhibited two zones: a discrete band of strong MLC
138 proximally to the edge, and a band of lower MLC signal distally to the edge that exhibits
139 a sharp boundary where the transverse arcs disassemble (Figure 1C, separated by
140 yellow dotted lines). ARHGEF17 displayed a strikingly different pattern: absence of
141 signal in the lamellipodium with an increasing gradient that peaks in the low MLC edge
142 proximal region, at the region where disassembly of transverse arcs occurs. These
143 specific MLC and ARHGEF17 domains remain constant over time (Figure 1C). These
144 data reveals a dynamic ultrastructure of the lamella with regions in which the myosin
145 lattice adopts different densities, with ARHGEF17 prominently binding the edge distal
146 region with low MLC density where lamella disassembly occurs.

147

148 **ARHGEF17 oligomerizes in cluster arrays that correlate with different**
149 **actomyosin networks**

150

151 To better understand ARHGEF17 subcellular localisation within the lamella, we
152 imaged ARHGEF17 and MLC dynamics using structured illumination microscopy

153 (SIM). SIM's enhanced resolution revealed discrete ARHGEF17 punctate structures
154 of different fluorescence intensities that we refer to as clusters, which might involve
155 ARHGEF17 oligomerization through the C-terminal propeller domain (Mitin et al.,
156 2012) (Figure 2A). Most likely through ARHGEF17's actin binding domain, these
157 clusters colocalized with actomyosin structures, and assembled into higher order
158 arrays (Figure 2A-C). SIM resolved single myosin II filaments and their arrangement
159 as stacks (Hu et al., 2017; Quintanilla et al., 2023) (Figure 2B, Movie S2). We then
160 used an implementation of the Crocker-Grier centroid-finding algorithm (Crocker and
161 Grier, 1996) to locate and quantify blobs that represent the myosin filament heads
162 (Quintanilla et al., 2023) and the ARHGEF17 clusters, and measured distances
163 between the latter (Figure S1A). Quantification of the distance between neighboring
164 myosin filament heads, over the whole cell, revealed a distance of approximately 280
165 nm (Figure S1B), as previously observed (Hu et al., 2017; Quintanilla et al., 2024,
166 2023). ARHGEF17 clusters displayed a similar distance distribution (Figure S1B). The
167 distance between neighboring myosin filament heads and ARHGEF17 clusters was
168 190 nm, suggesting that ARHGEF17 binding to F-actin positions them closely to the
169 myosin filament heads (Figure S1B).
170 We then observed that the retrogradely flowing ARHGEF17 clusters displayed distinct
171 organization patterns that correlated with different spatial arrangements of the
172 actomyosin lattice. We first describe the different subcellular domains with specific
173 actomyosin lattice arrangement. As expected, myosin II filaments were mostly absent
174 from the lamellipodium (Figure 2B,C,D inset 1). In the edge proximal lamella region, a
175 band of high density interwoven network of myosin filaments was observed (Figure
176 2D, inset 2). This crosslinked network most likely emerges from myosin redistribution
177 to the branched lamellipodial actin that condenses into actin arcs (Burnette et al.,

178 2011). Further within the cell, in the edge distal lamella region, we observed a second
179 network of parallel myosin filaments with lower MLC density (Figure 2D inset 3). This
180 explains the subdivision of the lamella in two zones with different MLC densities
181 previously observed with confocal microscopy (Figure 1B,C). Confocal imaging of
182 MLC and pMLC revealed that the edge proximal lamella contained a strong pMLC
183 signal, while the edge distal lamella region contained much lower pMLC signals
184 (Figure 3A,B,C inset 1). High resolution analysis of the edge distal lamella revealed
185 that its parallel myosin arcs are decorated by sparse punctate pMLC puncta (Figure
186 3C inset 2). The cell center was mostly characterized by single myosin filaments that
187 occasionally assemble into arcs, the latter retaining discrete pMLC punta (Figure 3C
188 inset 3). Our blob quantification method revealed that the fluorescence intensities of
189 the MLC signals were higher in the edge proximal versus distal lamella regions, and
190 much lower in the cell center (Figure S1C-E). These results reveal that the lamella
191 contains two separate myosin networks: 1. in the edge proximal lamella region, the
192 myosin network adopts a highly interwoven structure and is under tension with high
193 phosphorylated MLC, 2. the edge distal lamella region consists of a network of linear
194 myosin filaments with mostly low tension. Here the myosin filaments's motor domain
195 might be trapped in a rigor state, and only act as a crosslinker without generation of
196 contractility.
197 Evaluation of ARHGEF17 signals in these different subcellular regions revealed that
198 ARHGEF17 forms arrays of clusters that exhibit increasing fluorescence intensities as
199 they are transported retrogradely (Figure 2D). Small ARHGEF17 puncta were
200 observed in the lamellipodium (Figure 2D, inset 1). In the edge proximal lamella region,
201 ARHGEF17 assembled into larger clusters that localized in between the crosslinked
202 myosin filaments (Figure 2D, inset 2). In the edge distal lamella region, ARHGEF17

203 clusters displayed a further increase in density and formed lattices that are parallel to
204 the myosin filament network (Figure 2D, inset 3). ARHGEF17 clusters form networks
205 suggesting that they bind multiple actin filaments simultaneously (Figure 2D, inset
206 3). Both myosin filaments and ARHGEF17 clusters defined a sharp boundary
207 between the low contractile lamella region and the cell center (Figure 2C, dotted line).
208 In the cell center, we observed homogeneous distribution of ARHGEF17 clusters of
209 lower intensity than those observed in the edge distal lamella (Figure 2D, inset 4).
210 Quantification of fluorescence intensities in detected blobs revealed that ARHGEF17
211 clusters in the contractile edge proximal have lower fluorescence intensity than those
212 present in the low-contractile lamella region and the cell center (Figure S1C-E). We
213 also evaluated the subcellular localization of ARHGEF17 with respect to F-actin and
214 the actin crosslinker α-actinin (Figure 3D-F) using confocal microscopy. In the
215 contractile edge proximal lamella region, α-actinin mostly bound to adhesions and
216 diffuse ARHGEF17 signal were observed (Figure 3F inset 1). In the low contractile
217 edge distal lamella region, we observed that ARHGEF17 clusters were colocalizing
218 with F-actin filaments but were mutually exclusive with α-actinin puncta where F-actin
219 filaments are crosslinked (Figure 3F inset 2). This is consistent with the ability of
220 ARHGEF17 to bind ATP-actin, mostly at the barbed-end (Mitin et al., 2012). We
221 summarize the interactions of ARHGEF17 with the actomyosin lattice in Figure S2.
222
223 **ARHGEF17 clusters flow with the retrograde actin flow and correlate with**
224 **disassembly of actomyosin transverse arcs in the lamella**
225
226 Timelapse SIM imaging revealed that ARHGEF17 clusters flowed back with the actin
227 retrograde flow (Figure 4A,B, Movie S2 and S3). During this process, we observed
228 that the transported ARHGEF17 clusters exhibited fission and fusion events (Figure

229 4A,B, Movie S3), and increased in fluorescence intensity (Figure S1D,E). The
230 correlation of ARHGEF17 transport by the actin retrograde flow, and the formation of
231 ARHGEF17 clusters of increasing fluorescence intensities while transported
232 centripetally strongly suggests a mechanism of advection that coalesces the
233 ARGEF17 clusters. This flow was interrupted by disassembly of the myosin filament
234 lattice in the lamella edge that faces the center of the cell (Figure 4C, Movie S4). An
235 additional confocal timelapse dataset documents how ARHGEF17 enrichment
236 correlates with transverse myosin arc disassembly (Figure S3, Movie S5). The high
237 density of myosin arrays in the contractile edge proximal lamella region (Movie S3,
238 upper panels) did not make it possible to quantify if a similar phenomenon occurs at
239 this location. To further quantify the dynamic self organization properties of MLC and
240 ARHGEF17, we evaluated the local correlation of the orientation of fluorescent signals
241 using a custom algorithm inspired by the orientationJ plugin (Püspöki et al., 2016).
242 This was performed for both channels independently. We observed that while the
243 myosin lattice exhibited aligned arcs throughout the lamella, the characteristic aligned
244 ARHGEF17 arrays were mostly observed in the edge distal lamella part at sites where
245 transverse actomyosin arcs disassemble (Figure 4D, Movie S6). In the cell center,
246 small ordered myosin arcs interacted with ARHGEF17 cluster lattices which led to their
247 immediate disassembly (Figure 4E). These datasets suggest the actomyosin
248 retrograde flow dynamically organizes the advection and coalescence of ARHGEF17
249 clusters so as to concentrate the latter in transverse actomyosin arcs in the non-
250 contractile lamella. This can also occur on actomyosin arcs transiently occurring in the
251 cell center. When this spatially organizing mechanism of ARHGEF17 concentration
252 exceeds a specific threshold, ARHGEF17 might activate the RhoA-Rho associated
253 protein kinase (ROCK)-MLC activation to locally fracture the low contractile transverse

254 arcs leading to their disassembly. Thus local activation of RhoA through this spatially
255 organizing mechanism might lead to an opposite effect than reinforcement of
256 contractility which is usually the expected output of the Rho ROCK pathway.
257
258 **ARHGEF17 loss of function leads to loss of actomyosin disassembly**
259
260 To further evaluate ARHGEF17's function, we performed RNA interference KD
261 experiments, and evaluated F-actin, MLC phosphorylation and focal adhesion outputs
262 during REF52 spreading (Figure 5A). We observed a KD efficiency of 88 % at mRNA
263 level (Figure S4). To quantify these datasets, we built an image analysis pipeline to
264 automatically segment cells and measure fluorescence intensity as a function of
265 distance to the cell border (depicted in Figure S5A,B, see intensity profile analysis in
266 methods section). During cell spreading, *ARHGEF17* KD cells displayed a prominent
267 increase in F-actin signals in the edge distal lamella region (Figure 5A,B). This was
268 accompanied by robust increase in focal adhesion size and intensity, which are
269 hallmarks of high contractility. Surprisingly, this phenotype was only accompanied with
270 a modest increase in phosphorylated pMLC given these robust contractile responses
271 (Figure 5B). Time-lapse imaging of F-actin dynamics of *ARHGEF17* KD cells starting
272 from the onset of cell spreading revealed that the latter remain spread longer than their
273 control counterparts (Figure 5C, quantified in Figure 5D - area measurements, Movie
274 S7). Further, *ARHGEF17* KD cells lacked the ability of symmetry breaking much longer
275 than control cells, despite displaying a more contractile cytoskeleton (quantified in
276 Figure 5D - solidity measurements). At a time point of approximately 12 hours, we
277 observed that *ARHGEF17* KD cells display a very contractile actomyosin network with
278 respect to their control counterparts (Figure 5C - 12 hours). To better understand the
279 nature of the increased tension in the lamella cytoskeletal network in response to

280 *ARHGEF17* KD, we imaged MLC using SIM. We observed increased stacking of
281 myosin filaments in *ARHGEF17* KD cells in both the edge proximal and edge distal
282 lamella, with the density of myosin filaments decreasing in the edge distal lamella
283 region for both conditions (Figure 5E, quantified in Figure S5C). These results reveal
284 that loss of function of the RhoA-specific GEF ARHGEF17, leads to loss of actomyosin
285 disassembly in the edge distal non-contractile lamella. This leads to high contractility,
286 as observed at the level of F-actin and focal adhesions, in presence of only a small
287 increase in pMLC. After initial spreading, *ARHGEF17* KD cells display strong and
288 exceptionally stable contractile arcs which might explain the lack of the ability to break
289 symmetry for cell polarization. After multiple hours, *ARHGEF17* KD cells display an
290 extremely contractile actomyosin network. SIM imaging reveals that *ARHGEF17* KD
291 cells display increased stacking of myosin filaments. Together with the finding that
292 ARHGEF17 recruitment to the actomyosin lattice leads to its disassembly (Figure 3),
293 these results indicate that ARHGEF17 regulates disassembly of actomyosin networks
294 in the non contractile edge distal lamella.
295
296 **ARHGEF17 loss of function decreases RhoA activity in the edge distal lamella**
297
298 To evaluate how ARHGEF17 spatio-temporally regulates RhoA, we evaluated the
299 effect of ARHGEF17 loss of function on RhoA activation patterns as measured by the
300 FRET biosensor RhoA2G (Fritz et al., 2013). We simultaneously imaged F-actin
301 dynamics using the lifeact construct. In spreading REF52 cells, we observed that as
302 previously described (Martin et al., 2016, 2014), RhoA activity displays a focused
303 region of RhoA activity directly at the leading edge, of similar size than the
304 lamellipodium and the contractile edge proximal lamella as observed in Figure 3A-C
305 (Figure 6, Movie S8). This was followed by a zone of lower RhoA activity (Figure 6A).

306 As observed in figure 5A, *ARHGEF17* KD cells displayed an intense F-actin signal in
307 the edge distal lamella, due to lack of their disassembly. In these cells, the edge
308 localized RhoA activity pool remained unchanged, but lower RhoA activity correlated
309 with lack of F-actin network disassembly in the edge distal lamella (particularly visible
310 in the kymographs in figure 6B). Quantification by radially averaging RhoA activity
311 across the periphery of the cell (Figure 6C,D) revealed that the RhoA activity pool at
312 the edge remained unchanged, while the RhoA activity pool in the edge distal lamella
313 is lower in perturbed versus control cells. Global RhoA activity levels did not change
314 between control and perturbed cells, indicating that a very small pool of RhoA activity
315 is affected by *ARHGEF17* KD (Figure 6E). The finding that both RhoA activity (Figure
316 6) and pMLC signals (Figure 5) remain present in the edge proximal lamella in
317 *ARHGEF17* KD cells strongly suggests that this specific RhoA activity pool regulates
318 lamellar contractility. The low contractile edge distal lamella might then emerge
319 through retrograde flow in absence of RhoA-ROCK mediated MLC phosphorylation.
320 The finding of lower RhoA activity in the edge distal lamella, that correlates with
321 absence of F-actin network disassembly, indicates that ARHGEF17 regulates this
322 specific RhoA activity pool. Thus, two spatio-temporal RhoA activity pools, one in the
323 edge proximal and one in the edge distal lamella exist, and regulate actomyosin
324 assembly and disassembly respectively.

325

326 **ARHGEF17 preferentially binds to relaxing actomyosin networks**

327

328 The striking localisation of ARHGEF17 at myosin arcs, especially in the edge distal
329 low contractile lamella, strongly suggests that ARHGEF17 binds to relaxed,
330 disassembling myosin arcs (Figure 4). To orthogonally test this hypothesis, we used
331 an optogenetic system to locally transiently activate Rho to evoke a temporary pulse

332 of contractility followed by relaxation, and evaluate resulting ARHGEF17 dynamics.
333 We used a re-engineered optoLARG actuator consisting of a nano SspB domain for
334 efficient light-dependent recruitment of the LARG GEF domain to the iLID domain that
335 was fused to a low diffusing stargazin membrane anchor (Heydasch et al., 2023)
336 (Figure 7A). This construct was stably expressed at low levels together with
337 ARHGEF17-mCherry and lifeact-miRFP F-actin (Figure 7A). Illumination of a spot with
338 blue light led to local contractility as evidenced by accumulation of F-actin (Figure 7B,
339 Movie S9). After blue light removal, contractility rapidly disappeared. Kymograph
340 analysis revealed that ARHGEF17 was specifically binding to relaxing actomyosin
341 networks. To further corroborate this finding, we imaged ARHGEF17 dynamics in
342 response to myosin network relaxation triggered by Y-27632-mediated ROCK
343 inhibition (Figure 7C, Movie S10). We found that after ROCK inhibition ARHGEF17
344 was immediately recruited to the relaxing actomyosin network until it eventually
345 completely disassembled. Together, these results strengthen the idea that
346 ARHGEF17 selectively senses and binds to actomyosin arrays that are in a state of
347 relaxation.

348 **Discussion**

349 While assembly of actomyosin contractile systems has been extensively studied, their
350 disassembly remains virtually unexplored. It is currently assumed that cessation of
351 Rho/ROCK signaling, which leads to activation of myosin light chain phosphatase
352 (Amano et al., 2010) is sufficient for actomyosin network disassembly. Here we report
353 on a spatio-temporal signaling system dedicated to lamella disassembly. We show
354 that ARHGEF17 recruitment the low contractile, edge distal region of the lamella,
355 locally activates RhoA, and leads to its disassembly (Figure 8). This challenges the

356 commonly accepted notion that RhoA is a sole regulator of the assembly of
357 actomyosin networks. This underscores the need to understand Rho GTPase
358 signaling in time and space and is consistent with the hypothesis of spatio-temporal
359 signaling modules in which one GTPase can be spatially controlled by specific GEFs
360 and GAPs to perform different functions in time and space (Pertz, 2010). A model on
361 how ARHGEF17 regulates the disassembly of the lamellar actomyosin network is
362 depicted in Figure 8.
363
364 An important component of this spatio-temporal signaling system is the mechanism
365 by which ARHGEF17 is dynamically recruited to the lamella back region. SIM imaging
366 of myosin networks and ARHGEF17 dynamics indicate that ARHGEF17 is transported
367 backward with the actin retrograde flow (Figure 4A,B). This must involve the N-terminal
368 domain of ARHGEF17 that shows high selectivity for ATP-actin, and thus barbed ends
369 of F-actin filaments within the actomyosin lattice (Mitin et al., 2012) (Figure 8A). We
370 observe that during this process ARHGEF17 clusters form through fusion-fission
371 events (Figure 4A,B) and grow in size while they are transported centripetally (Figure
372 2, quantified in Figure S1C-E). This ultimately leads to highest ARHGEF17 density of
373 linear transverse arcs in the edge distal lamella where the latter disassembles (Figures
374 2, 4C, S2, Movies S3-S4). Formation of ARHGEF17 clusters most likely involve the
375 C-terminal β-propeller domain (Mitin et al., 2012), a domain regulating oligomerization
376 in multiple proteins such as clathrin (Wood and Smith, 2021) or Cdc20 and Cdh1 that
377 are involved in the activation of the anaphase-promoting complex/cyclosome during
378 cell division (Peters, 2006). The observation that ARHGEF17 clusters bear similar size
379 features than myosin filaments (Figure S1B), strongly suggest that these clusters
380 contain tens of ARHGEF17 molecules. Our live imaging data suggests that
381 ARHGEF17 clusters grow through an advection mechanism through interaction with

382 F-actin filaments during retrograde flow. Note that ARHGEF17 also contains a PH
383 domain that has been documented to bind to membranes (Mitin et al., 2012). Confining
384 ARHGEF17 transport to a 2 dimensional mechanism might feed into this advection
385 mechanism. An open question is why ARHGEF17 does not efficiently bind actin
386 barbed ends in the lamellipodium. We speculate that interactions with F-actin together
387 with the advection mechanism are necessary for concentration of ARHGEF17 clusters
388 in the back lamella region. Once ARHGEF17 clusters disassemble together with the
389 transverse myosin arcs in the distal lamella, they persist as disordered clusters in the
390 cell center (Figure 2D, quantified in Figure S1C-E) where they control disassembly of
391 spurious actomyosin networks in the cell center (Figure 4C).
392
393 Another important aspect of our spatio-temporal signaling system is how ARHGEF17
394 leads to actomyosin network disassembly during cell spreading. As just mentioned
395 above, ARHGEF17 interactions allow its dynamic accumulation at the lamella back
396 region where it correlates with actomyosin network disassembly (Figure 4).
397 ARHGEF17 KD experiments (Figure 5) as well as FRET experiments indicated that
398 ARHGEF17 regulates actomyosin disassembly through a RhoA-dependent
399 mechanism (Figure 6). How does this work ? We propose that local application of
400 tension through ARHGEF17/RhoA/ROCK might fracture transverse arcs in the lamella
401 back leading to their disassembly. This is consistent with *in vitro* (Murrell and Gardel,
402 2012) and *in vivo* (Wilson et al., 2010) evidence that myosin contractility can
403 disassemble actin networks. This mechanism might be further influenced by the
404 following factors: 1. Build-up of robust ARHGEF17 clusters might allow for a critical
405 concentration of local ARHGEF17 to efficiently locally switch ON RhoA activity; 2. the
406 position of ARHGEF17 clusters at the barbed end of F-actin filaments, away from α-
407 actinin mediated crosslinks which are crucial for stability of actomyosin networks

408 (Dwyer et al., 2022), might be an advantageous weak point to fracture the transverse
409 myosin arcs through local application of tension (Figure 8); 3. prominent ARHGEF17
410 clusters specifically localize within the low contractile edge distal lamella in which
411 myosins might only act as crosslinkers, which might be easier to fracture (Figure 8B);
412 4. low contractile actomyosin networks in the edge distal lamella might already be
413 prone to disassembly, producing new barbed ends for actin polymerization, ATP-actin
414 incorporation, and thus further ARHGEF17 recruitment. Our optogenetic and drug
415 perturbations of contractility (Figure 7) specifically illustrate the last point - during an
416 optogenetically-evoked contractility transient, ARHGEF17 specifically binds to
417 relaxing actomyosin networks (Figure 7A,B). Here, disassembling myosin networks
418 might produce barbed ends that can incorporate ATP-actin, and recruit ARHGEF17
419 that provides a positive feedback by locally and transiently evoking RhoA-mediated
420 contractility. An identical scenario applies to our ROCK inhibition studies (Figure 7C).
421 Thus, the self-organization properties of ARHGEF17, that involve interaction with
422 ATP-actin at F-actin barbed ends, as well as oligomerization might allow for its
423 localization to low contractile, disassembling myosin networks at the lamella back
424 region, providing a positive feedback for their robust disassembly.
425
426 Our data reveals the existence of two spatially distinct RhoA activation zones at the
427 leading edge of the cell, the 1st regulating actomyosin assembly, and the 2nd
428 regulating actomyosin disassembly. The 1st spatial pool of RhoA activity spans the
429 lamellipodium and the contractile edge proximal lamella region, displays high pMLC
430 signals (Figure 3A-C) and regulates actomyosin network assembly as already shown
431 before (Martin et al., 2016, 2014). Rac1 activity is also present at that location (Martin
432 et al., 2016), and RhoA activity might locally apply tension to lamellipodial branched
433 actin network to switch on actomyosin retrograde flow. The finding that *ARHGEF17*

434 KD maintains the 1st spatial pool of RhoA (Figure 6) indicates that another GEF and
435 GAP must regulate it. Candidate RhoA-specific GEFs might be LARG and GEF-H1
436 that have been shown to regulate cytoskeletal responses in response to force
437 application to integrins (Guilluy et al., 2011). The precise mechanisms that shape this
438 focused RhoA activity pool remain to be discovered. The second ARHGEF17-
439 mediated spatial RhoA activity pool is less intense and spans the non-contractile edge
440 distal lamella region that displays sparse pMLC signals to regulate contractility for
441 actomyosin network disassembly. Through retrograde flow, the contractile actomyosin
442 network under tension in the 1st zone transitions in the 2nd zone of low RhoA activity,
443 and adopts a relaxed state in which myosin filaments only displaying sparse pMLC
444 signals, and thus most likely only acting as crosslinkers. This poorly disassembling
445 actomyosin network can then activate ARHGEF17-mediated contractility through the
446 mechanisms we have discussed above. Thus, two specific RhoA spatio-temporal
447 activity pools that are regulating the lamella through different self-organization logics,
448 with the ARHGEF17-regulated pool specifically dedicated for disassembly of
449 actomyosin networks. Note that these RhoA activity patterns are particularly difficult
450 to spatially resolve simply because active RhoA diffuses in the plasma membranes by
451 virtue of its C-terminal geranylgeranyl moiety. Consequently, it is not possible to
452 visualize ARHGEF17-mediated local MLC activation occurring at barbed ends in the
453 low contractile edge-distal lamella. A better understanding of these different spatio-
454 temporal RhoA activity pools will require single molecule imaging methods that have
455 been previously used to image Rho GTPase dynamics (Mehidi et al., 2019).
456
457 Our work exemplifies the function of spatio-temporal feedback regulation in Rho
458 GTPase signaling. Such feedback regulation is ubiquitous in Rho GTPase signaling,
459 and for now has been mostly shown to be responsible for shaping spatio-temporal

460 signaling patterns (Bement et al., 2024). In our work, the ARHGEF17 pathway can be
461 understood as a spatially-regulated positive feedback to ensure robust and irreversible
462 disassembly of actomyosin networks. This might be required for efficient homeostasis
463 of the actomyosin cytoskeleton warranting the absence of contractile instabilities that
464 might lead to actomyosin network buckling, fracturing, or the formation of aggregates
465 as observed in cell free systems (Ideses et al., 2018). Further illustrating the concept
466 that Rho GTPase feedback mechanisms are important for cellular homeostasis, we
467 have recently observed a similar positive feedback mechanism impinging on RhoA
468 activity that involves spatio-temporal regulation of the RhoGAP DLC1 at focal
469 adhesions (Heydasch et al., 2023). Here, the positive feedback emerges from a
470 mechanical input at focal adhesions, locally amplifies RhoA signaling, and is required
471 for irreversible focal adhesion disassembly. The finding that 30% of Rho GEFs/GAPs
472 bind to the cytoskeleton or adhesions (Müller et al., 2020) strongly suggests
473 widespread mechanisms of cytoskeletal to Rho GTPase feedback that might regulate
474 cytoskeletal homeostasis or Rho GTPase pattern formation (Bement et al., 2024).
475 Future elucidation of the role of GEFs and GAPs in spatio-temporal Rho GTPase
476 signaling will need to take into account the concept of feedback regulation.
477
478 **ONLINE METHODS**
479
480 **Cell Culture and Transfection**
481
482 Rat Embryo Fibroblast 52 (REF52) cells were cultured in Dubelcco's Modified Eagle
483 Medium with 4.5 g/L glucose, 10% 4mM L-Glutamine, and 100 U/mL
484 penicillin/streptomycin. Cells were grown at 37ºC and 5% CO2.

485 For transfection, REF52 cells (45000 per well) were seeded in a 6-well plate a day
486 before. Cells were transfection using Lipofectamine 3000 Reagent and following the
487 protocol (Thermo Fisher). Transfected cells were kept overnight and visualised the
488 next day.
489
490 **siRNA KD**
491
492 4 ul of Lipofectamine RNAiMax (Thermo) was added to 500 ul of Opti-MEM (Thermo)
493 and siPOOL solution for 3 nM final siRNA concentration. This mix was added to a well
494 of 6-well plate and reverse transfection was done by adding 120000 cells in 1.5 mL
495 medium volume in the well. After 24 hours, cells were re-seeded on glass bottom well
496 plates (Celvis) which were coated with 5 µg/ml of human plasma fibronectin purified
497 protein.
498
499 **DNA constructs**
500
501 The optoLARG construct used was: pB3.0-optoLARG-mVenus-SspB-p2A-stargazin-
502 mtq2-iLID, as described in Heydasch et al., 2023. ARHGEF17-mCherry construct was
503 provided by Olivier Rocks, and ARHGEF17-GFP construct was from addgene #58893.
504 MLC-mCherry, MLC-miRFP, LifeAct-miRFP and LifeAct-mNeonGreen were prepared
505 previously in the lab.
506
507 **Optogenetic Experiments**
508
509 REF-52 cells with optoLARG construct and LifeAct-miRFP were transfected with
510 ARHGEF17-mCherry (kindly provided by Olivier Rocks) and plated on glass bottom
511 well plates (Celvis) which were coated with 5 µg/mL of human plasma fibronectin
512 purified protein (Merck) for one hour at room temperature. Cells were seeded at 6000

513 cells/well into 12 well plates and allowed to attach for 12 hours. Before imaging,
514 FluoroBrite DMEM medium was added to the cells. NIS-Elements (Nikon) was used
515 on the microscope for observing ARHGEF17 and LifeAct dynamics. Optogenetic
516 stimulation was localized to specific regions using an Andor mosaic 3 DMD and the
517 ROIs were individually defined for the cells. The images were taken using a 60x oil
518 objective. mCherry-ARHGEF17 and miRFP-LifeAct were imaged for 20 cycles with 5
519 seconds time interval for baseline, then stimulation with blue light in the ROI for 65
520 cycles with 5 seconds time interval, followed by no stimulation acquisition with 5
521 seconds time interval.
522
523 **Immunofluorescence antibody staining**
524
525 Vinculin, pMLC, Phalloidin-Atto647N (1:200 dilution), Alexa-Fluor-conjugated
526 secondary antibodies (used as 1:1000) were from Molecular Probes. One hour after
527 seeding, cells were fixed with 0.2% cold paraformaldehyde for 10 min, washed with
528 1x PBS three times, permeabilized with 0.1% Triton X solution, washed again with 1x
529 PBS, and blocked for 30 min at RT with 2% BSA solution in PBS. Cells were incubated
530 overnight with the primary antibody, and then washed with 2% BSA solution in PBS
531 three times next day. Secondary antibody incubation was done for 1 hour at RT
532 followed by three washes with 1x PBS.
533
534 **Y-27632 washout experiment**
535
536 REF-52 cells with LifeAct-miRFP were transfected with ARHGEF17-mCherry and
537 seeded on a 24-well glass bottom plate coated with 5 μg/mL fibronectin. Cells were
538 allowed to attach for 12 hours and FluoroBrite DMEM medium was added later for

539 imaging. Live cell imaging was done for addition of Y-27632. mCherry-ARHGEF17
540 and miRFP-LifeAct were imaged for 20 cycles with 5 seconds time interval for baseline
541 and then 32 µm of Y-27632 was added. Imaging was continued with 5 seconds time
542 interval until complete disassembly of actomyosin.
543
544 **RNA Extraction**
545
546 Cells growing in a 6-well plate were rinsed with PBS and 1 mL TRI-Reagent per well
547 was added. After 3 minutes of incubation, cells were transferred to a 15 mL tube and
548 200 µL chloroform was added. The tube was vortexed for 30 seconds and kept
549 standing for 5 min at RT. After this it was centrifuged at maximum speed for 5 min in
550 a centrifuge pre-cooled to 4°C. For each sample, 2 µL glycogen (20 mg/mL) was
551 pipetted in fresh eppendorf tubes. From the centrifuged samples, 350 µL of upper
552 aqueous phase was carefully removed and transferred into the corresponding tube
553 containing glycogen. 600 µL of isopropanol was then added to each tube and mixed
554 by inversion. The tubes were kept for 10 min at RT and then centrifuged at 4°C at
555 maximal speed for 15 min. The supernatant was carefully removed and discarded.
556 The pellet was gently rinsed with 1 mL ethanol 80% (diluted with DEPC water). The
557 tube was centrifuged for 5 min at maximal speed and supernatant was discarded. The
558 pellet was left to dry for 15 min and then 40 µL DEPC water was used to dissolve the
559 pellet. The extracted RNA was kept on ice and concentration measured in a Nanodrop
560 spectrophotometer.
561
562 **Reverse Transcription and qPCR**
563
564 To reverse transcribe all polyadenylated mRNAs of a cell an oligo(dT) primer can be
565 used which hybridises to the poly(A) tails of the mRNAs. For primer annealing, for

566 each reaction, 5µg RNA + 1µl oligo (dT) primer 10µM were mixed and filled up to total
567 25 µl with water. This was incubated for 5 min at 75°C and then let stand at RT for 5
568 min. 25 µl of 2X reverse transcription complementation mix was prepared for each
569 sample. For 25 µl 2X RT mix, 10.9 µl H2O, 5 µl 10X Affinity-ScriptTM buffer, 5 µl 100
570 mM DTT, 2.5 µl dNTP Mix 10 mM each from NEB, 0.8 µl RNAse inhibitor (Dundee
571 Cell Products) and 0.8 µl Reverse Transcriptase (Affinity Script Kit,
572 Agilent/Stratagene) were mixed. The 25 µl 2X RT mix was added to each sample with
573 RNA and annealed oligo(dT) primer, total 50 µl per tube. This was incubated for 10
574 min at 25°C (primer extension), 40 min at 42°C (reverse transcription) and 20 min at
575 60°C (enzyme inactivation). The resulting cDNA can be stored at -20°C. For qPCR,
576 following primer pairs were used. GAPDH Fwd: GTCTCCTCTGACTTCAACAGCG,
577 GAPDH Rv: ACCACCCTGTTGCTGTAGCCAA, ARHGEF17 Fwd:
578 CATAGCTTCTCCCAACCGCA, ARHGEF17 Rv: AGGTACGCAGGAAAGCTCAC.
579 For 20 µl reaction, 10 µl of SYBR™ Green PCR Master Mix 1X (Thermo Fisher), 0.4
580 µl each of 10 mM Fwd and Rv primers, 15 ng of cDNA and water upto 20 µl were
581 mixed and added to qPCR plate. Following program was run: Enzyme activation at 95
582 °C 1 min (1 cycle), Denature at 95 °C during 3 sec, Anneal/Extend/Acquire at 60 ºC
583 15 sec. 40 cycles were done and data analysed.

584 **Structured illumination microscopy (SIM)**

585 8-well chambered slides (Ibidi) coated with 5 µg/mL fibronectin were used for live cell
586 imaging using SIM. REF-52 cells with MLC-mCherry were transfected with
587 ARHGEF17-GFP (addgene #58893) and seeded in 8-well chambered slide. 30 min
588 after seeding, FluoroBrite DMEM medium was added and cells were imaged using
589 63x oil objective using 488 and 561 laser. The interval time between images is

590 30 seconds. The processing of the acquired data was done using Zen 3.0 imaging
591 software. The SIM Imaging was done at the Center for Microscopy and Image Analysis
592 at the University of Zürich.

593 **RhoA activity FRET imaging**

594 8-well chambered slides were coated with 5 µg/mL fibronectin. REF52 cells were
595 seeded in Fluorobrite DMEM supplemented with 0.5% FBS, 0.5% BSA, L-glutamine
596 and P/S. After 1 h images were acquired on a Nikon Eclipse Ti inverted microscope
597 with a 60x Plan Apochromat Objective, using a Prim95B sCMOS camera with 2x2
598 pixel binning.

599 Donor and FRET channels were excited using a Lumencor Spectra X 440 nm LED
600 and imaged sequentially with excitation filters 430/24 and a Dichroic Q465 long-pass
601 filter. For donor emission, a 480/40 nm bandpass filter was used, and for FRET
602 emission, a 535/30 nm bandpass filter was used.

603 Data was analyzed with custom python code with the pipeline described in (Spiering
604 et al., 2013).

605 **Image analysis**

606 Standard Python libraries were used for data processing and visualization (NumPy
607 1.24.4, pandas 2.0.3, skimage 0.22.0, Matplotlib 3.8.2).

608
609 *SIM cluster analysis (Figure S1 and S4C)*

610 For the analysis of clusters in SIM images in Figures 2 and 5, blob-like structures were
611 detected using the Crocker-Grier centroid-finding algorithm (Crocker and Grier, 1996)
612 implemented in the Python library Trackpy (version 0.6.1,

https://zenodo.org/records/7670439). The expected diameter was set to 3 pixels, and the image was inverted to match the input format expected by Trackpy. For the distance analysis, nearest neighbors were detected by constructing and parsing a KD tree, using the algorithm described in (Maneewongvatana and Mount, 1999), which is implemented in the Python library SciPy version 1.9.1 (Virtanen et al., 2020).

Linear structure enhancement and orientation analysis (Figure 4D,E)

Linear structures and their orientations were detected by convolving the image with a 2D Gabor filter bank (Granlund, 1978). For all pixels, the vector pointing towards a manually placed cell centroid was calculated, and the orientation was derived as an angle from this vector. This angle was then compared to the angle of the Gabor filter with the highest response. Aligned angles (more pointing towards the cell center) were colored in blue, while non-aligned angles (more parallel to the cell edge) were colored in red. Final visualization was done using an HSI (hue, saturation, intensity) model inspired by the software OrientationJ (Püspöki et al., 2016). The blue/red values were used as hue, the Gabor filter response as saturation, and the original image as intensity values. The code to reproduce the figure is available on github as a Jupyter notebook (https://github.com/hinderling/orientation-py).

Intensity profile analysis (Figure 5B)

Cells were segmented with Cellpose (Stringer and Pachitariu, 2024) using the cyto3 model, a diameter of 150 px, and Phalloidin and DAPI as input channels. Cells touching the image border were excluded from the analysis. A Euclidean distance transform was applied to the cell masks to find the distance from the cell border for each pixel. For each cell, pixels with the same distance were binned, and the mean intensity was calculated for all background-subtracted fluorescence channels. The first

60 pixels (~20 μm) were chosen for plotting. Cells with a shorter maximal distance were excluded from further analysis (mean maximal distance for all cells was 69.56 px).

Statistics

Statistics were computed with scipy (version 1.9.1).

Author contributions.

VR and OP conceptualized the paper, VR and BG performed experiments, BG and LH performed data analyses and wrote code, JVU built the optogenetic toolkit, VR and OP wrote the paper.

Acknowledgements.

We thank Daniel Riveline, Karsten Kruse, Damian Brunner and Miguel Vicente-Manzanares for constructive comments on the manuscript. We are grateful to Oliver Rocks for providing constructs, and Judith Trüb for help with cloning. We are grateful to the Microscopy Imaging Center of the University of Bern (https://www.mic.unibe.ch) and the Center for Microscopy and Image Analysis of the University of Zurich (https://www.zmb.uzh.ch) for support. This work was supported by the Swiss National Science Foundation Sinergia grant CRSII5_183550 to OP.

Additional Information

The authors declare no competing interests.

667 **Supplemental Information.**

668
669 **Supplementary Movie legends.**

670
671 **Movie S1:** Spinning disc confocal time lapse movie of MLC and ARHGEF17 in
672 a spreading REF52 fibroblast. Scale bar: 10 µm. Time: minutes:seconds.

673
674 **Movie S2:** SIM movie of MLC-mCherry and ARHGEF17-GFP of a spreading REF52
675 cell. Scale bar: 10 µm. Time: minutes:seconds.

676
677 **Movie S3**: High magnification timeseries insets of ARHGEF17/MLC SIM movie S2
678 zooming on the edge proximal contractile (top panel corresponding to Figure 4A) and
679 edge distal non contractile (bottom panel corresponding to Figure 4B) lamella. Scale
680 bar: 1 µm. Time: minutes:seconds.

681
682 **Movie S4:** High magnification timeseries insets of ARHGEF17/MLC SIM movie S2,
683 relevant to Figure 4C. Direction of actomyosin flow : Top to bottom. Scale bar: 1 µm.
684 Time: minutes:seconds.

685
686 **Movie S5:** Additional example of MLC-miRFP and ARHGEF17-GFP dynamics during
687 myosin transverse arc disassembly relevant to Figure S2.
688 Scale bar: 10 µm. Time: minutes:seconds.

689
690 **Movie S6:** Quantification of MLC and ARHGEF17 lattice orientations using
691 orientation-py corresponding to Figure 4D. Scale bar: 10 µm. Time: minutes:seconds.

692
693 **Movie S7:** Epifluorescence time lapse movie of control and ARHGEF17 KD REF52
694 cells expressing the F-actin marker Lifeact-mNeonGreen. Scale bar = 20 µm. Time
695 hours:minutes.

Movie S8: FRET measurement of RhoA activation and F-actin dynamics in spreading control versus *ARHGEF17* KD REF52 cells. Scale bar = 10 μm. Time hours:minutes.

Movie S9: Optogenetic stimulation of a small ROI in REF52 cells expressing optoLARG, LifeAct-miRFP and ARHGEF17-mCherry. Scale bar = 10 μm. Time minutes:seconds.

Movie S10: ARHGEF17-mCherry and F-actin (LifeAct-mNeonGreen) dynamics before and after relaxation triggered by Y-27632 ROCK inhibition. Scale bar = 20 μm. Time minutes:seconds.

References

Amano M, Nakayama M, Kaibuchi K. 2010. Rho-kinase/ROCK: A key regulator of the cytoskeleton and cell polarity. *Cytoskeleton* 67:545–554. doi:10.1002/cm.20472

Bement WM, Goryachev AB, Miller AL, von Dassow G. 2024. Patterning of the cell cortex by Rho GTPases. *Nat Rev Mol Cell Biol* 25:290–308. doi:10.1038/s41580-023-00682-z

Burnette DT, Manley S, Sengupta P, Sougrat R, Davidson MW, Kachar B, Lippincott-Schwartz J. 2011. A role for actin arcs in the leading-edge advance of migrating cells. *Nat Cell Biol* 13:371–382. doi:10.1038/ncb2205

Crocker JC, Grier DG. 1996. Methods of Digital Video Microscopy for Colloidal Studies. *J Colloid Interface Sci* 179:298–310. doi:10.1006/jcis.1996.0217

Dwyer ME, Robertson-Anderson RM, Gurmessa BJ. 2022. Nonlinear Microscale Mechanics of Actin Networks Governed by Coupling of Filament Crosslinking and Stabilization. *Polymers* 14:4980. doi:10.3390/polym14224980

723 Etienne-Manneville S, Hall A. 2002. Rho GTPases in cell biology. *Nature* 420:629–
724 635.
725 Fritz RD, Pertz O. 2016. The dynamics of spatio-temporal Rho GTPase signaling:
726 formation of signaling patterns. *F1000Research* 5.
727 doi:10.12688/f1000research.7370.1
728 Granlund GH. 1978. In search of a general picture processing operator. *Comput Graph*
729 *Image Process* 8:155–173. doi:10.1016/0146-664X(78)90047-3
730 Guilluy C, Swaminathan V, Garcia-Mata R, O'Brien ET, Superfine R, Burridge K. 2011.
731 The Rho GEFs LARG and GEF-H1 regulate the mechanical response to force on
732 integrins. *Nat Cell Biol* 13:722–727. doi:10.1038/ncb2254
733 Heydasch M, Hinderling L, Van Unen J, Dobrzynski M, Pertz O. 2023. GTPase
734 activating protein DLC1 spatio-temporally regulates Rho signaling.
735 doi:10.7554/eLife.90305.1
736 Hu S, Dasbiswas K, Guo Z, Tee Y-H, Thiagarajan V, Hersen P, Chew T-L, Safran SA,
737 Zaidel-Bar R, Bershadsky AD. 2017. Long-range self-organization of cytoskeletal
738 myosin II filament stacks. *Nat Cell Biol* 19:133–141. doi:10.1038/ncb3466
739 Ideses Y, Erukhmovitch V, Brand R, Jourdain D, Salmeron Hernandez J, Gabinet U,
740 Safran SA, Kruse K, Bernheim-Groswasser A. 2018. Spontaneous buckling of
741 contractile poroelastic actomyosin sheets. *Nat Commun*.
742 Itoh RE, Kurokawa K, Ohba Y, Yoshizaki H, Mochizuki N, Matsuda M. 2002. Activation
743 of Rac and Cdc42 Video Imaged by Fluorescent Resonance Energy Transfer-Based
744 Single-Molecule Probes in the Membrane of Living Cells. *Mol Cell Biol* 22:6582–6591.
745 doi:10.1128/MCB.22.18.6582-6591.2002
746 Kraynov VS, Chamberlain C, Bokoch GM, Schwartz MA, Slabaugh S, Hahn KM. 2000.
747 Localized Rac activation dynamics visualized in living cells. *Science* 290:333–337.

748 Machacek M, Hodgson L, Welch C, Elliott H, Pertz O, Nalbant P, Abell A, Johnson GL,
749 Hahn KM, Danuser G. 2009. Coordination of Rho GTPase activities during cell
750 protrusion. *Nature* 461:99–103. doi:10.1038/nature08242
751 Maneewongvatana S, Mount DM. 1999. Analysis of approximate nearest neighbor
752 searching with clustered point sets. doi:10.48550/arXiv.cs/9901013
753 Martin K, Reimann A, Fritz RD, Ryu H, Jeon NL, Pertz O. 2016. Spatio-temporal co-
754 ordination of RhoA, Rac1 and Cdc42 activation during prototypical edge protrusion
755 and retraction dynamics. *Sci Rep* 6:21901. doi:10.1038/srep21901
756 Martin K, Vilela M, Jeon NL, Danuser G, Pertz O. 2014. A growth factor-induced,
757 spatially organizing cytoskeletal module enables rapid and persistent fibroblast
758 migration. *Dev Cell* 30:701–716. doi:10.1016/j.devcel.2014.07.022
759 Mehidi A, Rossier O, Schaks M, Chazeau A, Binamé F, Remorino A, Coppey M,
760 Karatas Z, Sibarita J-B, Rottner K, Moreau V, Giannone G. 2019. Transient Activations
761 of Rac1 at the Lamellipodium Tip Trigger Membrane Protrusion. *Curr Biol* 29:2852-
762 2866.e5. doi:10.1016/j.cub.2019.07.035
763 Mitin N, Rossman KL, Currin R, Anne S, Marshall TW, Bear JE, Bautch VL, Der CJ.
764 2013. The RhoGEF TEM4 Regulates Endothelial Cell Migration by Suppressing
765 Actomyosin Contractility. *PLoS ONE* 8:e66260. doi:10.1371/journal.pone.0066260
766 Mitin N, Rossman KL, Der CJ. 2012. Identification of a Novel Actin-Binding Domain
767 within the Rho Guanine Nucleotide Exchange Factor TEM4. *PLoS ONE* 7:e41876.
768 doi:10.1371/journal.pone.0041876
769 Müller PM, Rademacher J, Bagshaw RD, Wortmann C, Barth C, van Unen J, Alp KM,
770 Giudice G, Eccles RL, Heinrich LE, Pascual-Vargas P, Sanchez-Castro M,
771 Brandenburg L, Mbamalu G, Tucholska M, Spatt L, Czajkowski MT, Welke R-W,
772 Zhang S, Nguyen V, Rrustemi T, Trnka P, Freitag K, Larsen B, Popp O, Mertins P,

773 Gingras A-C, Roth FP, Colwill K, Bakal C, Pertz O, Pawson T, Petsalaki E, Rocks O.
774 2020. Systems analysis of RhoGEF and RhoGAP regulatory proteins reveals spatially
775 organized RAC1 signalling from integrin adhesions. *Nat Cell Biol* 22:498–511.
776 doi:10.1038/s41556-020-0488-x
777 Murrell MP, Gardel ML. 2012. F-actin buckling coordinates contractility and severing
778 in a biomimetic actomyosin cortex. *Proc Natl Acad Sci* 109:20820–20825.
779 doi:10.1073/pnas.1214753109
780 Nalbant P, Hodgson L, Kraynov V, Toutchkine A, Hahn KM. 2004. Activation of
781 endogenous Cdc42 visualized in living cells. *Science* 305:1615–1619.
782 Pertz O, Hodgson L, Klemke RL, Hahn KM. 2006. Spatiotemporal dynamics of RhoA
783 activity in migrating cells. *Nature* 440:1069–1072. doi:10.1038/nature04665
784 Peters J-M. 2006. The anaphase promoting complex/cyclosome: a machine designed
785 to destroy. *Nat Rev Mol Cell Biol* 7:644–656. doi:10.1038/nrm1988
786 Ponti A, Machacek M, Gupton SL, Waterman-Storer CM, Danuser G. 2004. Two
787 Distinct Actin Networks Drive the Protrusion of Migrating Cells. *Science* 305:1782–
788 1786. doi:10.1126/science.1100533
789 Püspöki Z, Storath M, Sage D, Unser M. 2016. Transforms and Operators for
790 Directional Bioimage Analysis: A Survey. *Adv Anat Embryol Cell Biol* 219:69–93.
791 doi:10.1007/978-3-319-28549-8_3
792 Quintanilla MA, Hammer JA, Beach JR. 2023. Non-muscle myosin 2 at a glance. *J*
793 *Cell Sci* 136:jcs260890. doi:10.1242/jcs.260890
794 Quintanilla MA, Patel H, Wu H, Sochacki KA, Chandrasekar S, Akamatsu M, Rotty JD,
795 Korobova F, Bear JE, Taraska JW, Oakes PW, Beach JR. 2024. Local monomer levels
796 and established filaments potentiate non-muscle myosin 2 assembly. *J Cell Biol*
797 223:e202305023. doi:10.1083/jcb.202305023

798 Rossman KL, Der CJ, Sondek J. 2005. GEF means go: turning on RHO GTPases with
799 guanine nucleotide-exchange factors. *Nat Rev Mol Cell Biol* 6:167–180.
800 Salbreux G, Charras G, Paluch E. 2012. Actin cortex mechanics and cellular
801 morphogenesis. *Trends Cell Biol* 22:536–545. doi:10.1016/j.tcb.2012.07.001
802 Small JV, Stradal T, Vignal E, Rottner K. 2002. The lamellipodium: where motility
803 begins. *Trends Cell Biol* 12:112–120. doi:10.1016/S0962-8924(01)02237-1

804 Spiering, D. *et al.* (2013) 'Quantitative ratiometric imaging of fret-biosensors in living
805 cells', *Methods in Cell Biology*, pp. 593–609. doi:10.1016/b978-0-12-407761-4.00025-
806 7.

807 Stringer C, Pachitariu M. 2024. Cellpose3: one-click image restoration for improved
808 cellular segmentation. doi:10.1101/2024.02.10.579780

809 Virtanen P, Gommers R, Oliphant TE, Haberland M, Reddy T, Cournapeau D,
810 Burovski E, Peterson P, Weckesser W, Bright J, van der Walt SJ, Brett M, Wilson J,
811 Millman KJ, Mayorov N, Nelson ARJ, Jones E, Kern R, Larson E, Carey CJ, Polat İ,
812 Feng Y, Moore EW, VanderPlas J, Laxalde D, Perktold J, Cimrman R, Henriksen I,
813 Quintero EA, Harris CR, Archibald AM, Ribeiro AH, Pedregosa F, van Mulbregt P.
814 2020. SciPy 1.0: fundamental algorithms for scientific computing in Python. *Nat*
815 *Methods* 17:261–272. doi:10.1038/s41592-019-0686-2
816 Wilson CA, Tsuchida MA, Allen GM, Barnhart EL, Applegate KT, Yam PT, Ji L, Keren
817 K, Danuser G, Theriot JA. 2010. Myosin II contributes to cell-scale actin network
818 treadmilling through network disassembly. *Nature* 465:373–377.
819 doi:10.1038/nature08994
820 Wood KM, Smith CJ. 2021. Clathrin: the molecular shape shifter. *Biochem J*
821 478:3099–3123. doi:10.1042/BCJ20200740

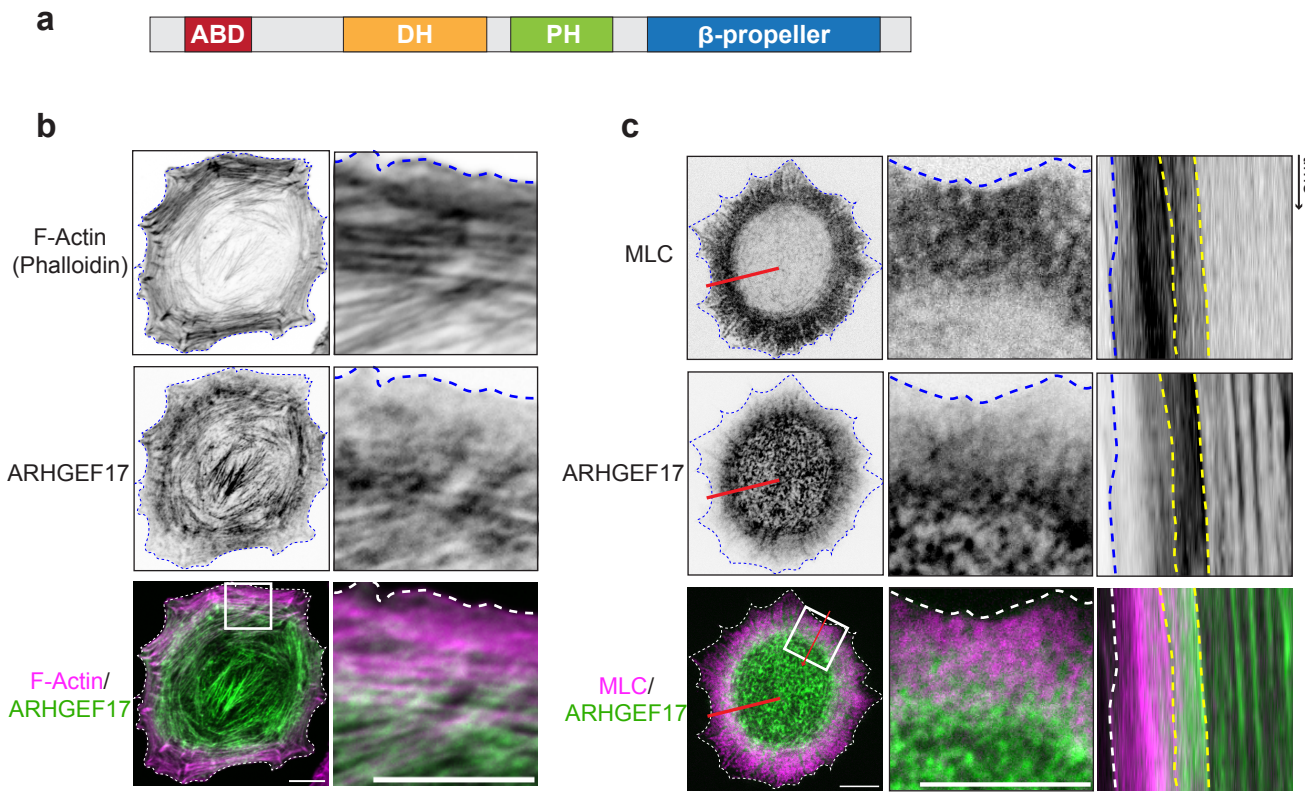

Figure 1. ARHGEF17 Structure, subcellular localization and dynamics
A: Scheme of the domain structure of ARHGEF17. (ABD : Actin Binding Domain)
B,C,D: Images are shown with inverted black and white contrast (ibw), or overlayed channel color-coded images are shown.
B: Confocal images of a spreading REF52 expressing ARHGEF17-mCherry and immunostained with Phalloidin. Left panels: whole cell. Right panels: magnified insets from boxes
C: Spinning disk confocal timelapse imaging of a spreading REF52 cell expressing ARHGEF17-GFP, and MLC-mCherry. Right panel: Kymograph analysis of both signals along the line drawn in red in the left panel.
Scale bars: 10 µm

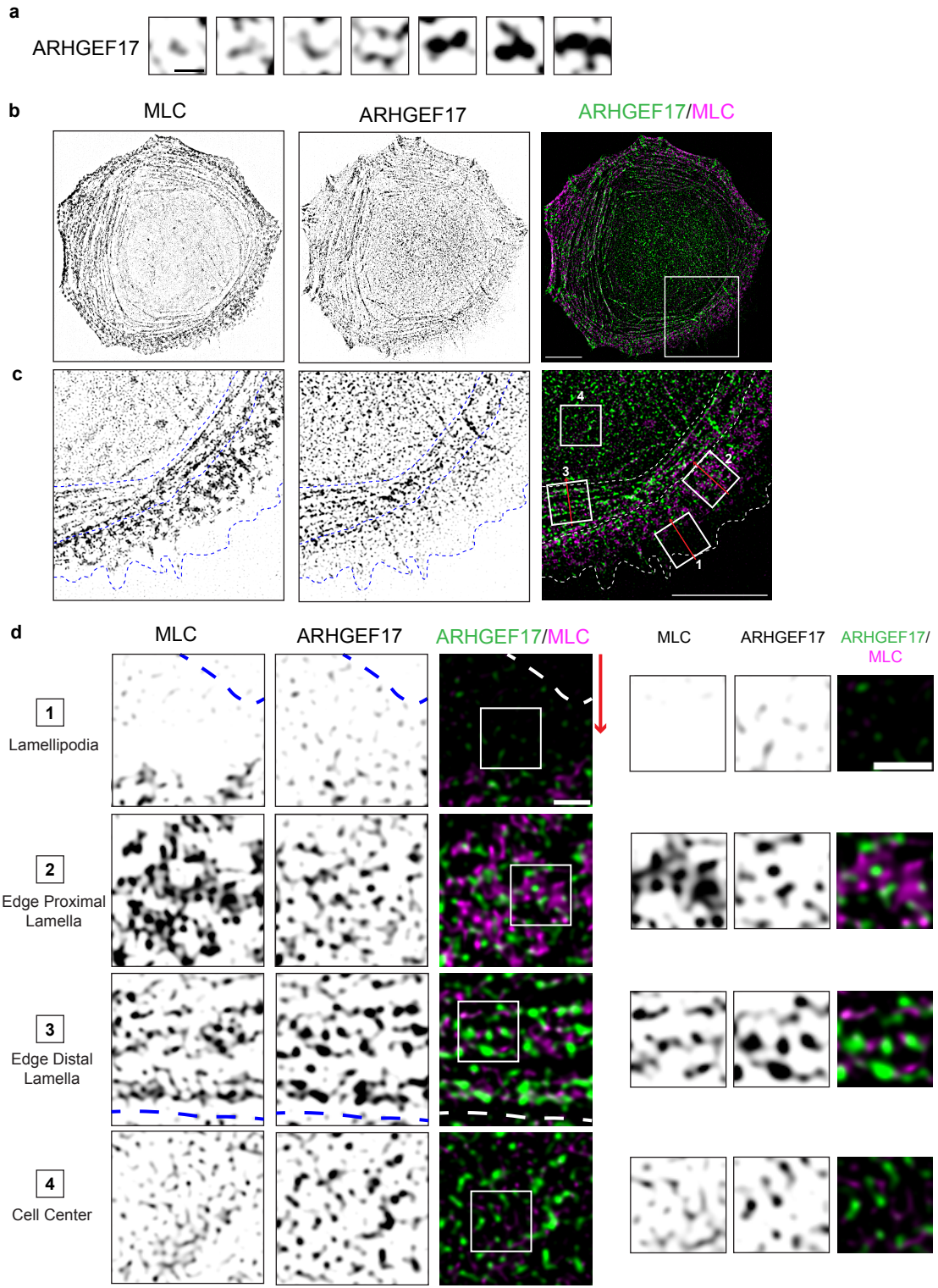

Figure 2: SIM imaging of ARHGEF17 and Myosin Light Chain subcellular localization.
All images come from SIM imaging of a spreading REF52 fibroblast expressing ARHGEF17-GFP and MLC-mCherry. Ibw of single channels or color-coded overlays are shown.
A: Gallery of ARHGEF17 clusters document their oligomerization properties.
B: ARHGEF17/MLC subcellular localization over the whole cell.

C: High magnification panel of A. Dotted lines delineate the cell edge, the interface between the contractile and low-contractile lamella regions, the low contractile lamella with the cell center.
D: High magnification panels from C. Note that the panels have been oriented to be parallel to the edge, with the retrograde actin flow being oriented from top to bottom (denoted by the red arrow). Additional magnified insets on the right panels provide intuition about the ultrastructure of the MLC and ARHGEF17 arrays. Inset 1: Lamellipodium, inset 2: edge proximal contractile lamella, inset 3: edge distal low contractile lamella, inset 4: cell center.
Scale bars: (A) 0.5 μm, (B,C) 10 μm, (D) 1 μm.

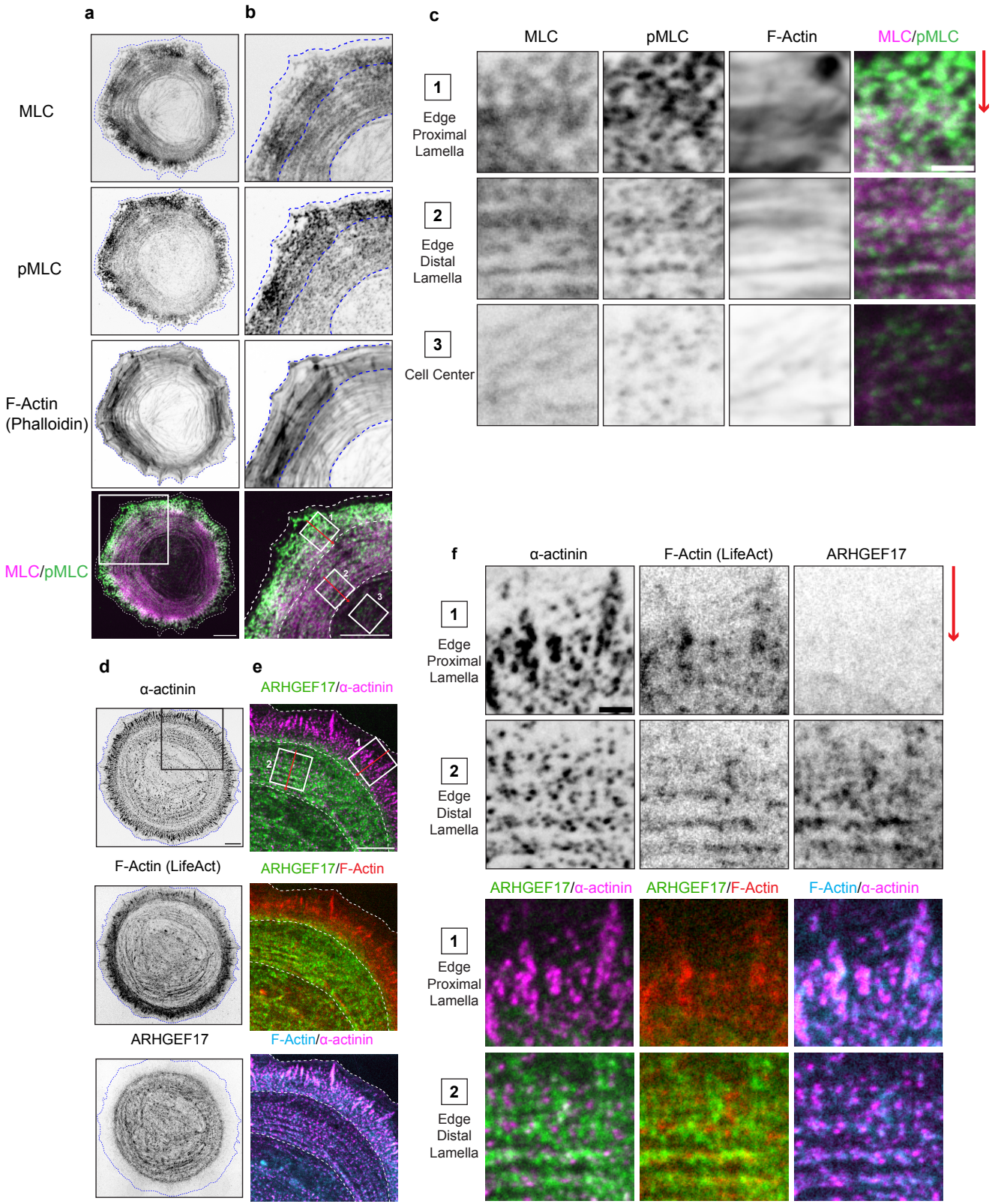

Figure 3: Subcellular localisation of MLC/MLC phosphorylation and ARHGEF17, F-actin and a α-actinin. A-C Confocal imaging of a spreading REF52 cell expressing MLC-mCherry and immunostained with pMLC and Phalloidin.

A: Global view of the cell
B: Magnification panel of the inset shown in (A)
C: High magnification panels of the insets shown in (B). Inset 1: edge proximal contractile lamella, inset 2: edge distal low contractile lamella, inset 3: cell center.
D-F: Confocal imaging of spreading REF52 cells expressing ARHGEF17-mCherry and LifeAct-miRFP and immunostained with α-actinin.
D: Global view of the cell
E: Magnification panel of the inset shown in (D)
F: High magnification panels of the insets shown in (E). Inset 1: edge proximal contractile lamella, inset 2: edge distal low contractile lamella
Ibw of single channels or color-coded overlays are shown. Note that the panels of (C) and (F) have been oriented to be parallel to the edge, with the retrograde actin flow being oriented from top to bottom (denoted by the red arrow).
Scale bars: (A-B) 10 µm, (C) 2 µm, (D) 10 µm, (F) 2 µm

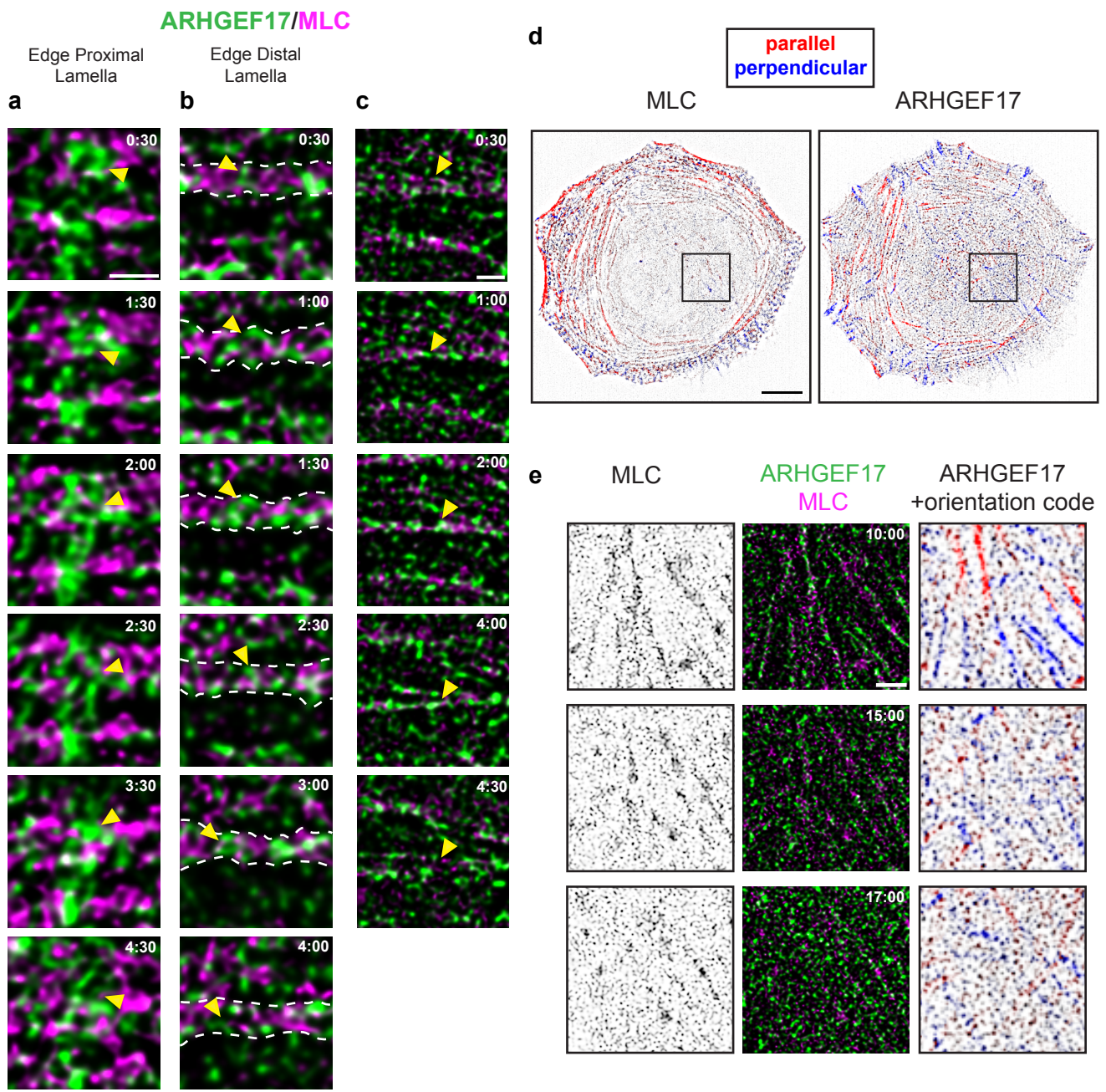

Figure 4: SIM imaging of ARHGEF17 and Myosin Light Chain dynamics.
SIM imaging
SIM timeseries of the same cell shown in Figure 2 are shown.
A,B: High resolution time series micrographs of ARHGEF17 and MLC dynamics in the edge proximal contractile (A) and edge distal low contractile lamella (B).
C: Timeseries micrographs of ARHGEF17 and MLC dynamics in the low contractile edge distal lamella with an example of transverse arc disassembly.
D: Analysis of correlated orientation of Myosin filaments (MLC) and ARHGEF17 clusters as analyzed using orientation-py. Correlated fluorescence signals that are parallel/perpendicular to the edge are color-coded in red and blue respectively. Ibw contrast is shown.
E: Timeseries micrographs of the disassembly of an actomyosin fiber in the cell center by ARHGEF17. Left panel: MLC (Ibw contrats), Middle panel: ARGEF17/MLC overlay, right panel: ARHGEF17 + orientation code.
Scale bars: (A-B-C) 1 µm, (D) 10 µm, (E) 2 µm

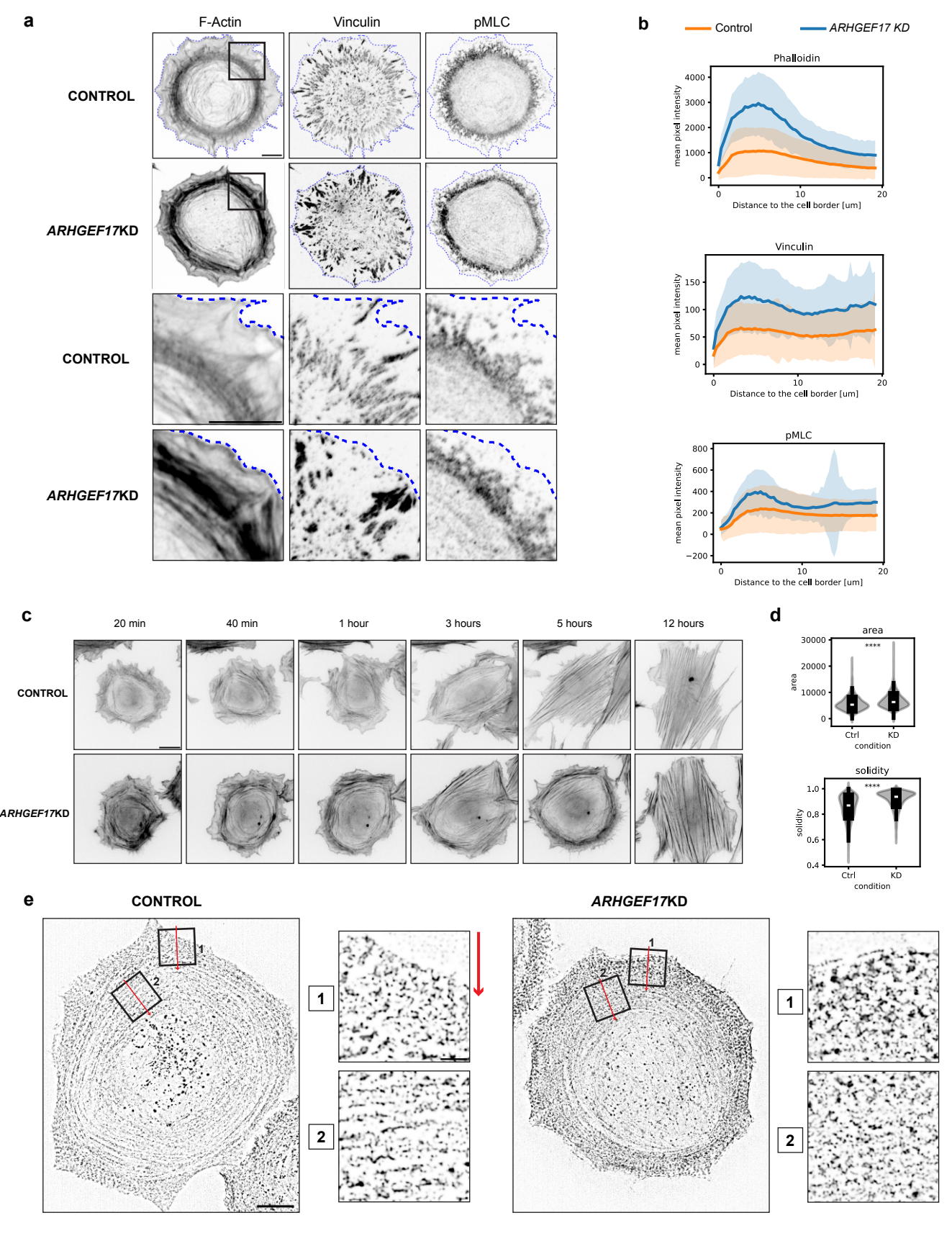
a
F-Actin
Vinculin
pMLC
CONTROL
ARHGEF17KD
CONTROL
ARHGEF17KD
b
Control
ARHGEF17 KD
Phalloidin
mean pixel intensity
Distance to the cell border [um]
Vinculin
mean pixel intensity
Distance to the cell border [um]
pMLC
mean pixel intensity
Distance to the cell border [um]
c
20 min
40 min
1 hour
3 hours
5 hours
12 hours
CONTROL
ARHGEF17KD
d
area
****
area
Ctrl
KD
condition
solidity
****
solidity
Ctrl
KD
condition
e
CONTROL
ARHGEF17KD
1
2
1
2
1
2
1
2

Figure 5: Effects of ARHGEF17 siRNA KD in REF52 cells

A: Fluorescence micrographs of cells stained with Phalloidin (F-actin), Vinculin and pMLC specific antibodies showing the impact of ARHGEF17 KD on cell morphology during spreading. Cells were detached, allowed to spread for 1 hour on fibronectin-coated coverslips. Images acquired using a 100x planApo oil immersion objective.

B: Quantification of phalloidin, pMLC and vinculin fluorescence intensities in control and ARHGEF17 KD cells (Images acquired using a 100x objective). Distance intensity plots are shown for intensity of staining from cell border towards cell center. Shaded area indicates standard deviation. n= 477 cells (242 Control, 235 KD).

C: Time-lapse series showing cell spreading and polarisation in control versus ARHGEF17 KD cells. Increased spreading and robust contractile F-actin structures are noted in KD cells within the first five hours as compared to control cells. At 12 hours, thicker contractile fibers are observed in ARHGEF17 KD cells.

D: Quantitative analysis of area and solidity of control and KD cells after 5 hours of spreading, measured at time point 5 hours. Boxplot with interquartile ranges and superimposed violin plots are shown to provide an intuition about the measurement distributions. White bar indicates population average. n=2033 (945 Control, 1088 KD). Statistical test: Mann-Whitney U test.

E: SIM images of spreading cells expressing MLC-mCherry in control and ARHGEF17 KD cells. High magnification panels showing (1) MLC in edge proximal lamella (2) MLC in edge distal lamella. The panels have been oriented to be parallel to the edge, with the retrograde actin flow being oriented from top to bottom (denoted by the red arrow).

Scale bars : (A) 10 µm, (C) 5 µm, (E) 10 µm, (E) Insets: 2 µm

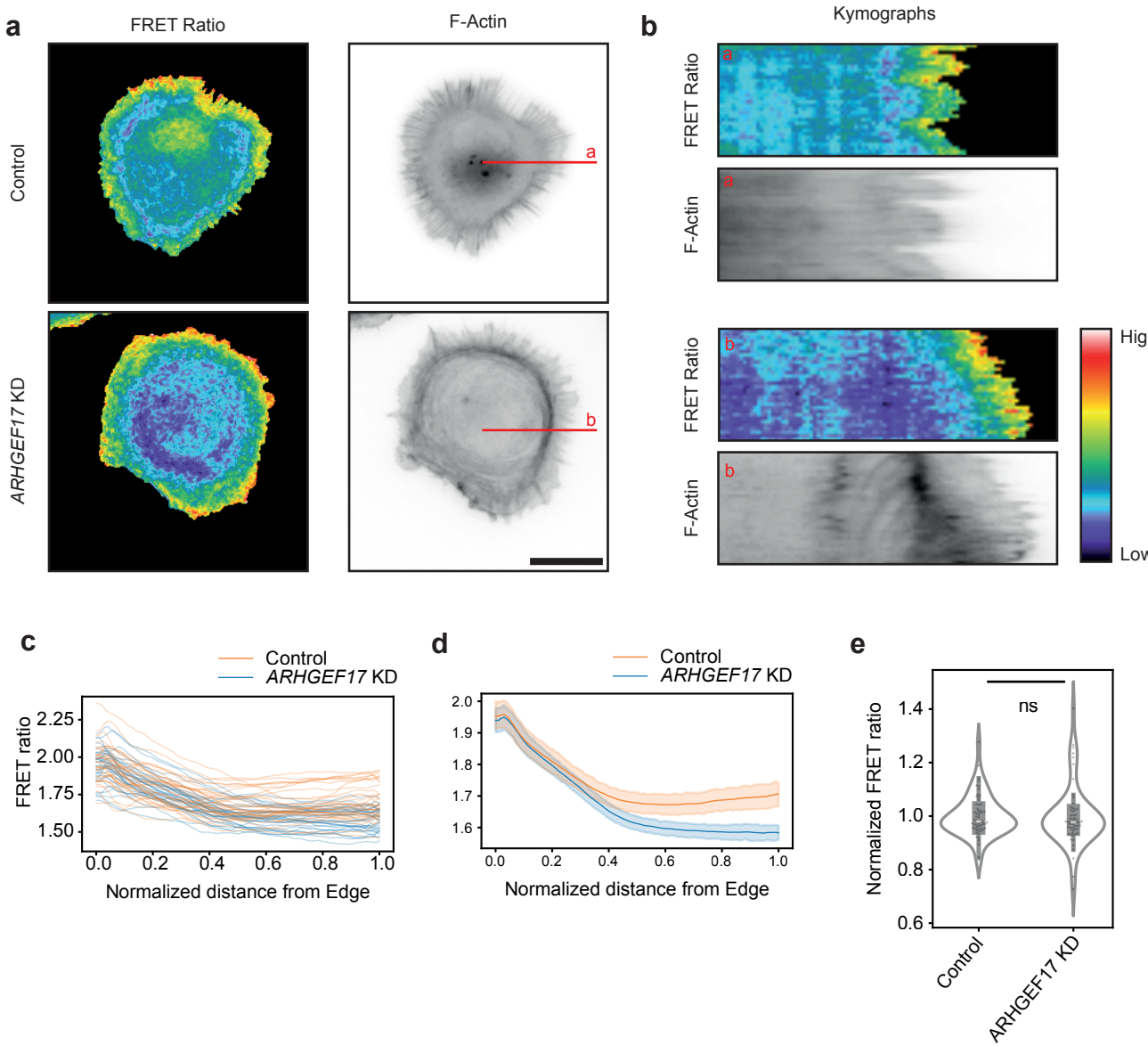

Figure 6: RhoA activity patterns in control versus ARHGEF17 KD cells.
A: Ratio images of RhoA2G FRET signals and Lifeact-mCherry F-actin in control versus ARHGEF17 KD cells. Ratio images are color-coded according to the color scale shown in (B). Lifeact-mcherry image is shown in inverted black and white contrast.
B: Kymograph analysis of the image in (A) along the red line.
C: Distance intensity RhoA FRET ratio plots are shown for single cell (see material and methods image analysis section). n=34 cells per condition.
D: Averaged distance RhoA FRET ratio plots. n=34 cells per condition. Shaded region indicates 95% confidence interval.
E: Measurements of RhoA FRET ratio cell averages. Measurements are normalized to the median value of the control. A t-test was used to assess statistical significance.
Scale Bar: (A) 50 µm.

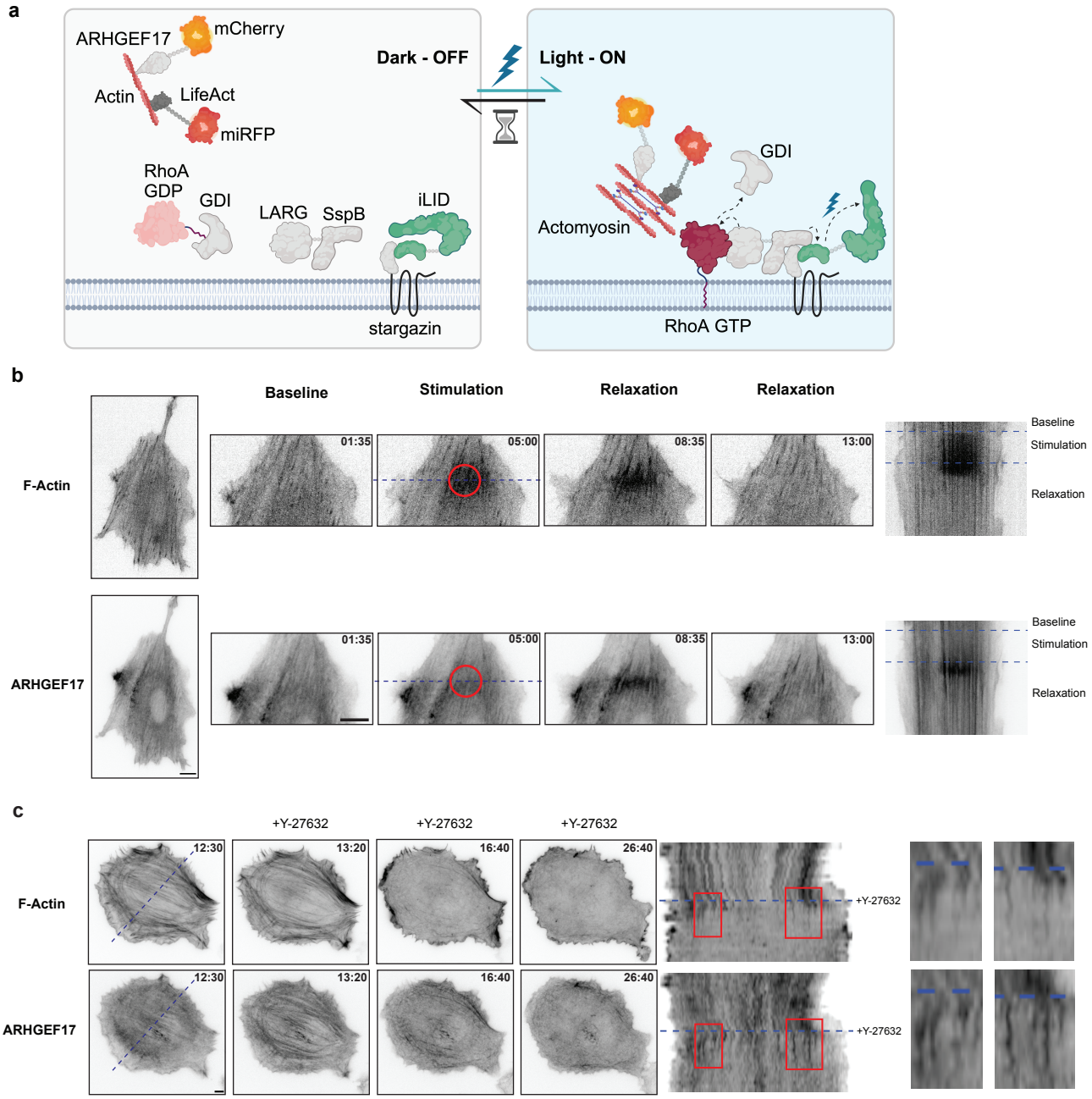

Figure 7: Mechanosensitivity of ARHGEF17 interaction with Actomyosin Network
A: Diagram of the optogenetic setup to study ARHGEF17 dynamics in response to a pulse of contractility. OptoLARG is an ILID-based optogenetic actuator to locally control Rho-mediated contractility and can be used with spectrally orthogonal mCherry tagged ARHGEF17 and the F-actin marker LifeAct-miRFP (adapted from Heydasch et al., 2023).
B: Cells activated locally by blue light to induce actomyosin contraction and relaxation, illustrating ARHGEF17 binding during actomyosin disassembly rather than assembly. Time in mm:ss.
C: Observations under ROCK kinase inhibitor Y-27632, showing ARHGEF17 transiently binds to disassembling actomyosin network. Time in mm:ss
Scale bars: (B-C) 10 µm

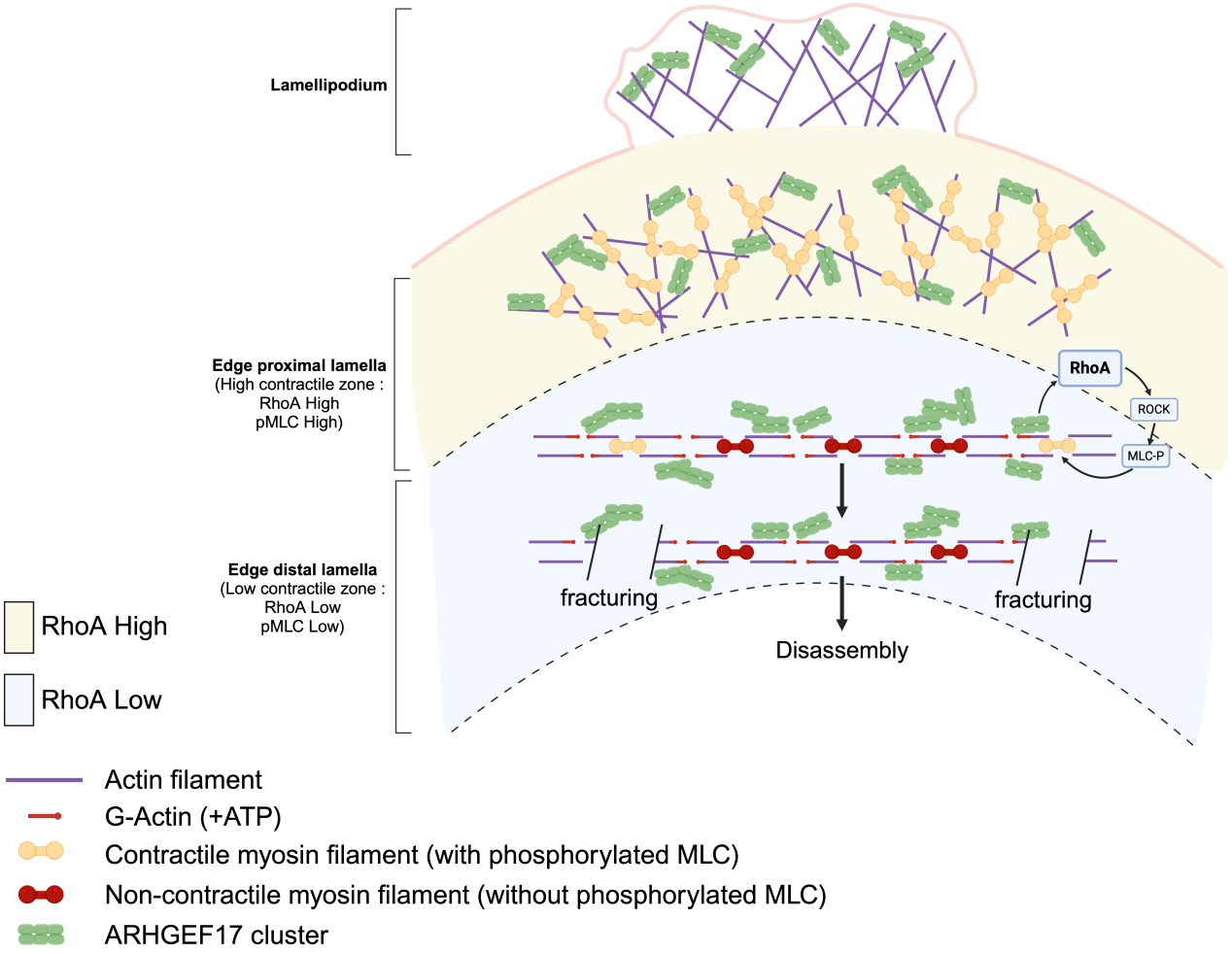

Figure 8: Model of ARHGEF17-mediated spatio-temporal regulation of lamella actomyosin network disassembly.
Note that all myosin filaments and ARHGEF17 clusters are shown so as not to overload the model.
1. ARHGEF17 clusters start to interact with F-actin filaments in the lamellipodium and are transported backwards with the actomyosin retrograde flow. ARHGEF17 clusters most likely interaction with ATP-actin at barbed ends.
2. In the edge proximal lamella, RhoA activity regulated by GEFs/GAPs that remain to be discovered induce MLC phosphorylation through activation of ROCK, resulting in strong actomyosin contractility. ARHGEF17 clusters continue to be transported backwards, and increase in density through an advection mechanism.
3. In the edge distal lamella, the actomyosin network relaxes because it transitions into the region of lower RhoA activity, leading to MLC dephosphorylation. Most myosin filaments most likely only act as crosslinkers, without exerting tension. ARHGEF17 localizes to barbed ends of F-actin filaments crosslinked by both non contractile myosin filaments and alpha-actinin. High ARHGEF17 concentration locally applied to the non contractile actomyosin network leads to its disassembly, most likely by fracturing the actomyosin lattice.